ORIGINAL ARTICLE



Multiphysics modeling of in situ integration of directed energy deposition with ultrasonic nanocrystal surface modification

Kishore Mysore Nagaraja¹ · Wei Li¹ · Dong Qian¹ · Vijay Vasudevan² · Youngsik Pyun³ · Hongbing Lu¹

Received: 14 December 2021 / Accepted: 21 March 2022 / Published online: 29 March 2022 © The Author(s), under exclusive licence to Springer-Verlag London Ltd., part of Springer Nature 2022

Abstract

In this paper, an in situ integration of the laser-assisted powder-based directed energy deposition (DED) process with a post-processing surface engineering technique called an ultrasonic nanocrystal surface modification (UNSM) is presented and analyzed with a multiphysics computational approach. The goal of this integrated process is to improve the quality of the DED built part by mitigating the high magnitude tensile residual stress in the built layer by incorporating compressive residual stress. The multiphysics, multi-scale computational modeling approach involves a meso-scale computational fluid dynamics (CFD) model interfaced with a macro-scale finite element method (FEM). The CFD model simulates powder feeding, transient thermal gradient, heat transfer, and laser-assisted powder-based DED melt pool dynamics. This model is then coupled with FEM to evaluate the effect of the UNSM process on the residual stress. The simulation results show that UNSM incorporates compressive residual stress to a depth of ~800 μm for a single built layer of ~1100 μm and shifts a region with an average of ~170 MPa tensile residual stress into one with an average of ~600 MPa compressive stress.

 $\textbf{Keywords} \ \ Directed \ energy \ deposition \cdot Ultrasonic \ nanocrystal \ surface \ modification \cdot Residual \ stress \cdot Computational \ fluid \ dynamics \cdot Finite \ element \ method$

1 Introduction

The laser-assisted powder-based directed energy deposition (DED) process uses a coaxial nozzle to inject the metallic powder using an inert gas flow at its periphery along with a high-power laser beam path at the center [1]. The fully or partially melted powders interact with the laser during deposition onto a substrate surface, resulting in a transient temperature gradient [2, 3], which influences the evolution and accumulation of the tensile residual stress and the thermal distortion in the final part [4–6]. The residual stress formed during and after the deposition process is further influenced

- Wei Li
 Wei.Li@UTDallas.edu
- ☑ Dong QianDong.Qian@UTDallas.edu
- Department of Mechanical Engineering, The University of Texas at Dallas, Richardson, TX, USA
- Department of Material Science and Engineering, University of North Texas, Denton, TX, USA
- Department of Mechanical Engineering, Sun Moon University, Asan, Korea

by the re-melting, and re-solidification of the successive layers. This could accelerate the growth of micro-cracks and contribute to the higher internal stress under the application of external loads [7–9].

To mitigate the tensile residual stress, several researchers have investigated the process parameters of the DED process such as scanning strategy, building structures including a substrate, and the support structures [10–16]. It has been shown that the residual stress can be mitigated by reducing the local temperature gradient and improving the surface finish at the melt pool region during metal deposition [17–20]. However, it is difficult to optimize the process for this purpose due to the dependence of residual stress on numerous unknown quantities and uncertainties.

A few post-processing techniques used to reduce the residual stress in the machined components are extended to AM processes. These include shot peening, heat treatment processes [21], laser shock peening [22–25], electron beam irradiation, rolling, and others to strengthen the surface hardness of the components [26–29]. For example, research by Kalentics et al. [30–34] studied the effect of laser shock peening (LSP) on the tensile residual stress in the SLM-built layers. LSP is applied on the



SLM-built steel samples using a decoupled approach. In this approach, the samples need to be moved back and forth from the SLM machine to the LSP station which makes it both time-consuming and difficult to control.

Furthermore, the application of these techniques to DED poses challenges, as some of these techniques alter dimensions of the deposited layers, and require precise control of the heat treatment conditions. In addition, it is nearly impossible to treat all the layers and their local melt pool regions using those techniques. Moreover, they are best suited for subtractively manufactured components and are yet to be explored in-depth for additive manufacturing which is a layer-by-layer deposition technique. Hence, in this work, we report a novel hybrid AM process based on in situ integration of a surface treatment technique called ultrasonic nanocrystal surface modification (UNSM) with the DED process as shown in Fig. 1.

In UNSM treatment, severe plastic deformation is induced onto the material surface under a combination of static and dynamic force components [35, 36]. This generates a fine surface texture and improves wear resistance, surface roughness, and fatigue strength [37–40]. It has been shown that UNSM generates deeper residual stress and gradient nanostructures compared to other post-processing techniques such as ultrasonic shot peening, and laser shock peening methods [41].

Due to the small footprint of the UNSM process unit, it can be installed inside the DED process space, leading to an in- situ integrated process. The process consists of alternating steps of DED and UNSM, all of which are performed in situ; i.e., there is no need to completely stop one process, remove the part, subject it to another process, and then put it back to restart. This integration brings in two major benefits: (1) It significantly reduces the production cycle, thus improving productivity. (2) It allows for more precise control of the part quality due to the close coupling of these processes.

Fig. 1 Schematic representation of an in situ integration of the UNSM surface engineering technique with the DED AM process wherein the UNSM process is applied over the DEDed layer during the deposition

The effects of UNSM on DED-built steel surfaces were studied by Kim et al. [42-44], using an experimentation approach. They found that hardness was improved up to 400 µm depth, and the surface roughness and waviness can be tailored through UNSM process parameters such as static load and scanning speed. Sidhu [45] studied the effect of UNSM on the selective laser melting process and found that UNSM has induced compressive residual stress as high as 975 MPa in SLM-built Inconel 718. In their research, the UNSM process altered the tensile residual stress region to a compressive residual stress region and has an effective depth of ~530 µm. Cho et al. [46] studied the effect of the UNSM on laser-assisted direct metal deposited tool steel components in experiments. In the scanning direction, the average grain size of the deposited surface was improved after the UNSM treatment from 5–30 µm to 1–10 µm grain size. The UNSM process also increased the surface hardness from 21 to 34 HRC. However, in all the reported studies, UNSM is not directly integrated with the AM process. Furthermore, there have been no modeling studies on the effects of UNSM on AM-built parts. The present study will bridge the gap by an investigation of the effect of UNSM on the residual stress in a DED layer using a multi-scale computational framework. The modeling results will provide important insight into the nature of the residual stress evolution and accumulation in the DED single layer, and an in situ effect of the UNSM on the DED layer.

2 Simulation methodology

The proposed computational framework is shown in Fig. 2. It involves a meso-scale CFD modeling of the DED process, followed by validation by comparing the simulated DED layer surface morphology with published experimental data. The CFD model is then coupled with a macro-scale FEM

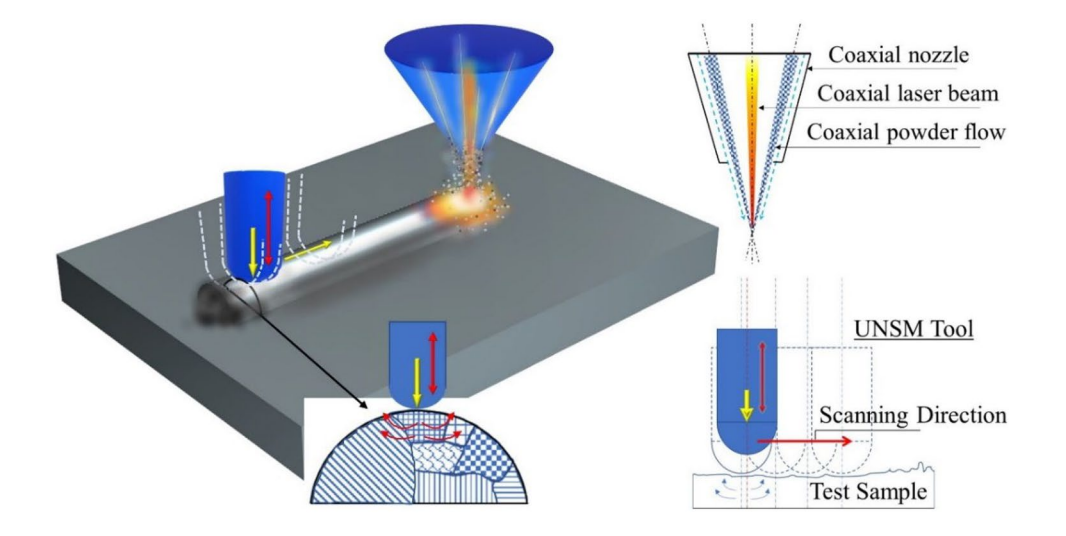
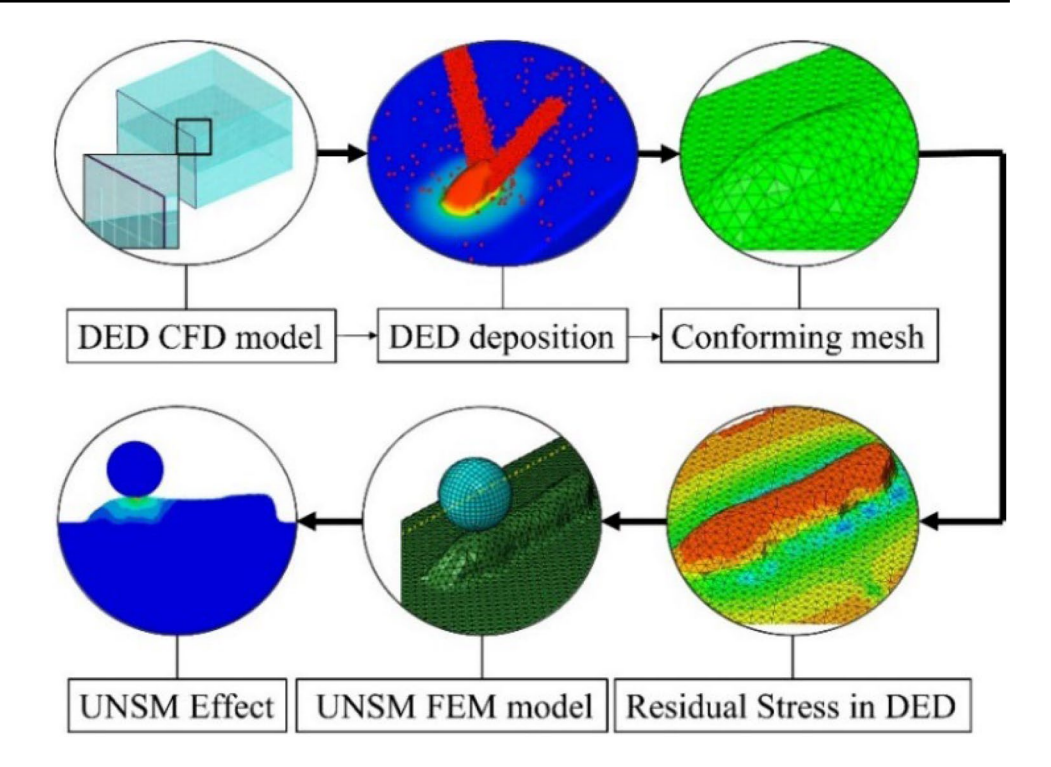




Fig. 2 Methodology for multiscale computational modeling of a hybrid powder-based DED-UNSM process



model to simulate the effect of the UNSM process on the residual stress evolution. The CFD-FEM coupling involves an interface modeling technique where the CFD spatial grids are converted into a CAD representation (STL mesh), which is further converted into a FEM tetrahedral mesh. This FEM mesh is then supplied with an input on the temperature distribution map from the CFD analysis.

The key advantage of this approach is that the conforming mesh is directly built from the CFD grid. This allows to accurately capture the surface profile (including surface roughness), internal voids, and partially melted particles obtained from the CFD analysis. An ability to consider these aspects is extremely important for predicting stress and defects. It is a significant improvement from the currently available standard quiet/inactive element approach.

2.1 Directed energy deposition model

2.1.1 DED simulation set-up

The directed energy deposition simulation involves a laser model and a coaxial nozzle that is presumed to have two entry points for powder feeding and the center in line with the laser path. The DED process parameters considered are provided in Table 1. In the next step, the CFD domain as shown in Fig. 3 is divided into two sub-regions. Fluid region 1 is air initially, and the deposition happens in this region and fluid region 2 is the substrate. These fluid regions have meshed with a grid size of $200~\mu m$.

Once the mesh is generated in the Cartesian frame, the *Y*-direction is set as the deposition direction, the *X*-direction is the in-plane perpendicular direction, and the *Z*-direction is the laser head location direction. The walls are modeled with symmetric boundary conditions, and *Z*-axis is loaded with 100 kPa pressure at 293 K temperature, and the domain is also assigned with fluid properties, thermal properties, and mechanical properties of the stainless steel 316L material [47], which are listed in Table 2.

The DED process involves melt pool generation, layer formation, and solidification of the layer, all of which are resolved by the CFD algorithm using Flow-3D 2022 R1 [48] that numerically solves the mass, momentum, and energy conservation equations with a finite volume approach [49–51]. Furthermore, the volume of fluid (VOF) technique is established for tracking and locating the fluid interfaces. In the CFD-VOF method, each cell of a mesh is assigned with a time-dependent fluid fraction step function F and only one value for each dependent variable is used to define the fluid state. The function F with a value of 1 represents the fluid region, 0 represents the non-fluid region, and in between represents the

Table 1 DED process parameters

Parameters	Value
Laser Power	225 W
Scanning speed	1000 mm/min
Laser spot size	2 mm
Laser diameter	2 mm
Absorptivity	35%



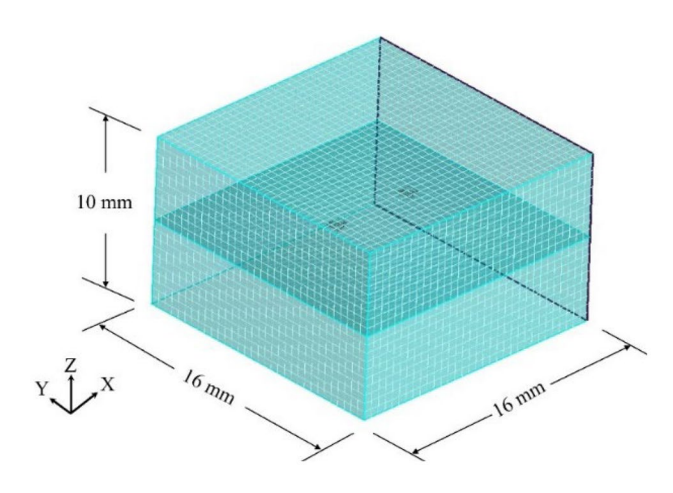


Fig. 3 The CFD domain created to deposit a single layer SS316L using a laser-assisted powder-based directed energy deposition process with two sub-regions and powder feeding sources

interface that must contain the free surface. It is governed by partial derivatives in the form of Eq. (1), which is further used to define the boundaries [52], where ν is the velocity vector.

$$\frac{\partial F}{\partial t} + \nabla \cdot (vF) = 0 \tag{1}$$

For each cell region, based on the information of F with its dependent variables such as velocities and pressures, conservations of momentum, energy, and mass (Eqs. (2)–(4)) are solved:

$$\frac{\partial \mathbf{v}}{\partial t} + (\mathbf{v} \cdot \nabla)\mathbf{v} = -\frac{1}{\rho}\nabla p + \mu \nabla^2 \mathbf{v} + \mathbf{g} + \mathbf{f}$$
 (2)

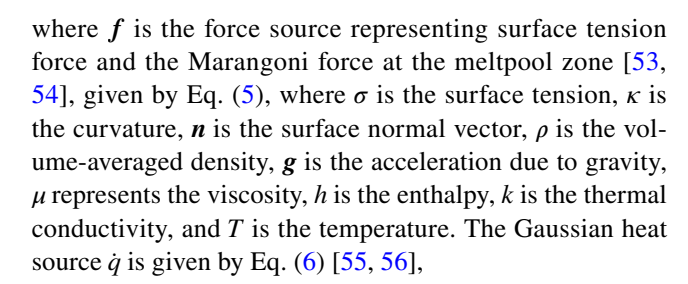
$$\frac{\partial h}{\partial t} + (v \cdot \nabla)h = -\frac{1}{\rho}\nabla \cdot k\nabla T + \dot{q} \tag{3}$$

$$(\nabla \cdot \mathbf{v}) = 0 \tag{4}$$

$$f = \left[\sigma\kappa n + \frac{d\sigma}{dT}(\nabla T - n(n \cdot \nabla T))\right] |\nabla F| \frac{2\rho}{\rho_{\text{metal}} + \rho_{\text{gas}}}$$
 (5)

Table 2 Properties of stainless steel 316L

Properties	Value
Density	7249 kg/m ³
Young's modulus	205 GPa
Specific heat	726 J/kg K
Thermal conductivity	28.95 W/m K
Solidus temperature	1673 K
Liquidus temperature	1697 K
Thermal expansion coefficient	$1.5 \times 10^{-5} \text{ K}^{-1}$



$$\dot{q}(r) = \frac{\eta P_{\text{laser}}}{\pi R^2} \exp\left(-\frac{2r^2}{R^2}\right) \tag{6}$$

where P_{laser} is the laser power, R is the laser radius, η is the absorptivity (or absorption rate) of the laser beam that depends on the laser wavelength and the material, and r is the spot radius.

Continuing further, the governing equations to describe the driving force on particle flow in DED are expressed in Eqs. (7)–(9). Since the initial velocity of a particle at the powder feeder inlet is a constant value, the particle velocity during the feeding process can be calculated. Therefore, the particle mass distribution during the feeding process will be determined.

$$m_i \frac{d^2 \mathbf{x}}{dt^2} = \mathbf{F}_{ij}^c + \mathbf{F}_i^f + \mathbf{F}_i^g \tag{7}$$

$$F_{i}^{f} = m_{i} \frac{18\mu}{\rho_{p} d_{p}^{2}} \frac{C_{D} R_{e}}{24} (\boldsymbol{u} - \boldsymbol{u}_{p})$$
(8)

$$\boldsymbol{F}_{i}^{g} = m_{i} \frac{g(\rho_{p} - \rho)}{\rho_{p}} \tag{9}$$

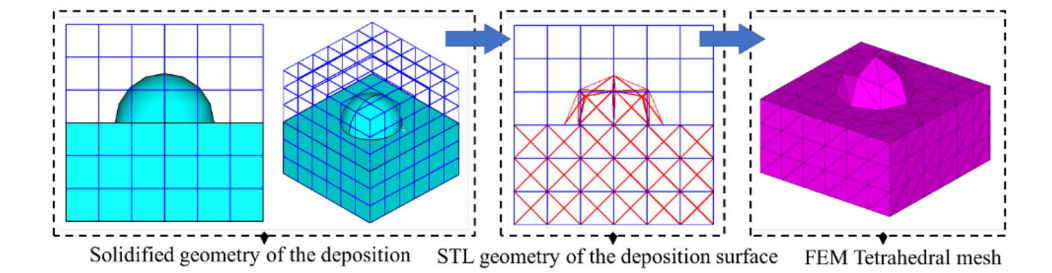
The force balance for a particle i is expressed in Eq. (7), where x denotes the translational displacement of the particle i. F_{ij}^c is the contact force acting on particle i by particle j or the walls. F_i^c is the gas drag force acting on particle i. F_i^g is the gravitational force. In Eq. (8), u_p , ρ_p and d_p are the velocity, density, and diameter of the particle, respectively. C_D is the drag coefficient which is a dimensionless quantity. R_e is the Reynolds number, and μ is the viscosity of gas flow. In Eq. (9), g is the gravitational acceleration.

2.2 Conforming mesh approach

An Eulerian–Lagrangian approach is developed to precisely mesh the complex geometries of the built component. In this implementation, a Lagrangian mesh is established based on the CFD-VOF simulations as shown in Fig. 4: First, the VOF method in the fluid solver provides detailed information on the surface profile of the deposited layer. These surface features will be represented by a surface triangular mesh (Standard Tessellation Language — STL format) that is commonly used for CAD (not to be confused with the FEM mesh introduced later).



Fig. 4 An illustration of the steps to establish a Lagrangian mesh based on results from CFD-VOF simulation



In the next step, the deposited layer will be discretized using finite element mesh based on the surface triangular mesh output from the CFD simulation. Once the Lagrangian mesh is constructed, the temperature values resolved at the center of the control volume in the thermal-fluid solver will be mapped to the FEM nodes using the standard FEM shape function interpolations. Compared with the existing quiet or inactive element methods, the proposed method significantly improves the accuracy of the surface representation and can also be extended to capture internal interfaces such as those due to porosity. These improvements will be demonstrated in numerical examples in the sequel.

2.3 Thermo-mechanical model

In the thermo-mechanical model, at first, CFD analysis is coupled to the thermo-mechanical FE model. Using the conforming mesh approach as described in Sect. 2.2, the temperature resolved from the CFD analysis at each time step is mapped to the Lagrangian finite element mesh to resolve the residual stress. It ensures the residual stress evolves as the irregular surface morphology evolves during the deposition. Once the DED simulation is completed, the CFD analysis is terminated, and the thermo-mechanical FE model will be employed to capture the residual stress due to both the temperature gradient and the applied UNSM load in the second step. In the constitutive model, stress σ will be solved as a function of the total strain ε , given as Eqs. (10)–(12). With C being the elasticity tensor, ε^e , ε^T , and ε^p are respectively the elastic, thermal, and plastic strains; α is the thermal expansion coefficient; and i is the second-order identity tensor.

$$\mathbf{\sigma} = \mathbf{C} : \boldsymbol{\varepsilon}^{\ell} \tag{10}$$

$$\varepsilon = \varepsilon^e + \varepsilon^T + \varepsilon^p \tag{11}$$

$$\varepsilon^T = \alpha \Delta T i \tag{12}$$

A temperature and rate-dependent Johnson–Cook model as shown in Eq. (13) is implemented to compute the plastic strain,

$$\overline{\sigma} = \left(A + B\left(\varepsilon_{\text{eff}}^{p}\right)^{n}\right) \left(1 + C\ln\left(\frac{\dot{\varepsilon}_{\text{eff}}}{\dot{\varepsilon}_{0}}\right)\right) \left(1 - \left[\frac{T - T_{0}}{T_{m} - T_{0}}\right]^{m}\right) \tag{13}$$

where $\overline{\sigma}$ represents the effective stress, $\varepsilon_{\rm eff}^P$ is the effective plastic strain, $\dot{\varepsilon}_{\rm eff}$ is the effective plastic strain rate, T is the temperature of the material, T_m is the melting point of the material, T_0 is the initial temperature, $\dot{\varepsilon}_0$ is the reference strain rate, and A, B, C, n, and m are the material constants listed in Table 3 [57].

2.4 Ultrasonic nanocrystal surface modification model

In general, the UNSM process involves the use of an ultrasound transducer to generate ultrasonic waves. The amplitude of these waves is to be amplified and then used to strike on the surface of the layer deposition through a tool called a strike pin which is usually made of Tungsten Carbide (WC). In the UNSM process, static and dynamic components of the strike force (load) can be independently adjusted to achieve desired enhancement goals for surface mechanical properties, and can be represented by Eq. (14),

$$F_m = F_s + F_a \sin(\omega t) \tag{14}$$

where F_s is the static load, F_a is the load produced by the transducer, ω is $2\pi f$, where f is the frequency (Hz), and F_m is the sum of the dynamic impact load and the static load.

In the UNSM finite element modeling using the commercial finite element code Dassault Systèmes [58], the WC tool is modeled as a rigid body. This tool strikes the top surface of the DED layer at an ultrasonic frequency. The UNSM process parameters are mentioned in the Table 4. Using the standard experimental tool configuration, the tool is modeled as spherical with a 2.38-mm diameter and is discretized with the tetrahedral elements. The placement of the tool onto the surface of the DED layer is as shown in Fig. 5.

In the contact model, the DED built part geometry is considered as a target body and the tool geometry is considered as a rigid body. This allows a master-slave

Table 3 Johnson-Cook model parameters of SS316L

A	В	n	m	С	$\dot{\epsilon}_0$
305 MPa	1161 MPa	0.61	0.517	0.01	1.0/s



Table 4 UNSM process parameters

Parameters	Value
Static load	50 N
Dynamic frequency	20 kHz
Dynamic amplitude	5 mm

relationship for the contact constraints. The DED geometry is considered as a deformable body, and between these two, frictional contact with the frictional coefficient of 0.1 is established based on an experimental study [59] wherein authors have studied the tribological effect of UNSM on a single-phase austenite SS316L. The reported friction coefficient is in the range of 0.05-0.2 with a stable frictional coefficient for untreated SS316L ~0.14 and a UNSM treated SS316L ~0.12. The target body is modeled using 3D C3D4 elements, and the rigid body is modeled with 3D C3D8R elements. At first, the model is subjected to the static load to check the reaction force at the tip of the tool to study the effect of the static load on the UNSM tool. To execute this static step, the displacement controlled method is considered where the WC tool is made to first strike on the DED layered surface up to a depth of 25 µm to calculate the reaction force. Based on this reaction force and its corresponding time, the tool position and static component force inputs are calibrated for the subsequent dynamic model. More specifically, the static component force of 50 N is applied.

In the dynamic step, on top of the static force, a dynamic component in the form of an amplitude $a = A_0 + B\sin\omega t$ is added to the strike force and is simulated for 0.025 s. This results in 500 strikes on the DED layered surface. During the 0.025 s, the WC tool also undergoes a 1-mm translational

distance from its initial position. The base of the substrate is fixed in all 6 degrees of freedom, and the maximum time increment size of 1×10^{-5} s is set. Overall, the average CPU time consumed for each CFD simulation step for the DED process with a Dell Precision 7920 Workstation (Intel(R) Xeon(R) Platinum 8276 CPU at 2.20 GHz, 2.19 GHz with 32 GB memory) was ~1.05 min. Similarly, the average CPU time consumed for each FE simulation step for residual stress in DED build and the UNSM treatment process was ~3 min and ~3.7 min, respectively on a Dell PowerEdge R730 workstation (Intel E5-2670 processor at 2.3 GHz with 128 GB memory).

3 Results and discussion

3.1 Deposited geometry, temperature distribution, and meltpool formation

The calculated temperature distribution of the DED single layer deposition is shown in Fig. 6 (left). The deposited SS316L single layer is approximate ~0.8 cm in length and ~0.23 cm in width. At the end of the deposition process, the maximum temperature reached 1893 K, which is slightly higher than the liquidus temperature of 1713 K and the solidus temperature of 1663 K. During the deposition stage, the maximum temperature is several hundred K more than the melting temperature of the deposition material. It exceeds the melting temperature within 1/10th of a second. In between, the peak temperature of the deposition has reached 3385 K at the end of 70% of the layer deposited. These observations demonstrate the complex temperature profile which is dynamic and transient.

Fig. 5 The finite element modeling of the UNSM process on the DEDed single layer coupled with the CFD-VOF simulation

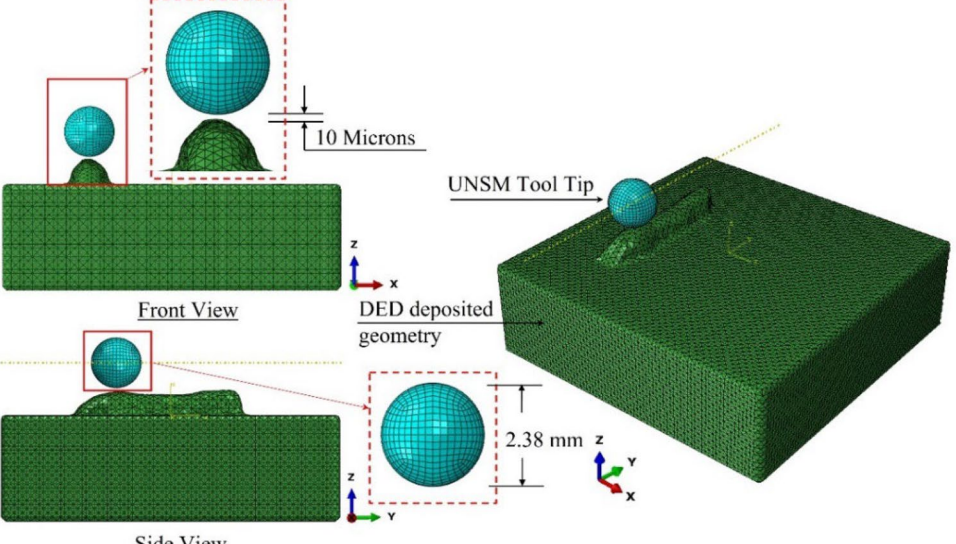
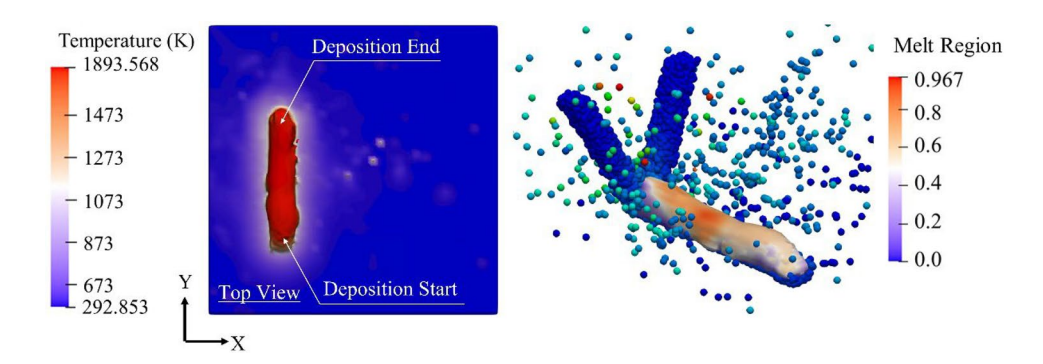






Fig. 6 The temperature distribution (left), powder flow, and meltpool formation (right) of the DEDed single layer SS316L depicting the complex surface profile of an over-dimension DED layer



Similarly, the interaction of the powder flow with the melt pool is shown in Fig. 6 (right). The steep temperature of the powder particles is observed near the melt pool region. Due to the focus point of the laser and the powder flow, which is just above the melt pool region, the peak temperature of the powder particles is higher than the melting temperature in the melt pool. This helps the melting of the powder particles and the formation of the melt pool region itself. In the melt pool region contours, the scale of 0 depicts the non-melted region, 1 refers to the fully melted region and in between refers to the molten region.

3.2 Experimental validation

The predicted irregular shape surface morphology is compared with the experimental observations for the same power source condition reported in the literature [60, 61].

The cross-sectional shape of the layer deposition from the simulation model (results extracted at the solidified region near the deposition starting location) and the experiment are shown in Fig. 7. The cross-section of the geometries between the simulated melt pool and the experimental melt pool geometry are compared using four dimensional parameters that are the height (H) from the substrate top surface, melt pool depth (h_d) onto the substrate, width (W), and the contact angle (α) between the substrate and the melt pool. These parameters are tabulated in Table 5, and a good agreement is observed.

3.3 The effect of ultrasonic nanocrystal surface modification on DED

After the deposition, the laser power is shut off, and the DED layer is allowed to cool down for 300 s. The steep

Fig. 7 Cross-sectional geometry comparison between the experiment [61] and the CFD-VOF simulation

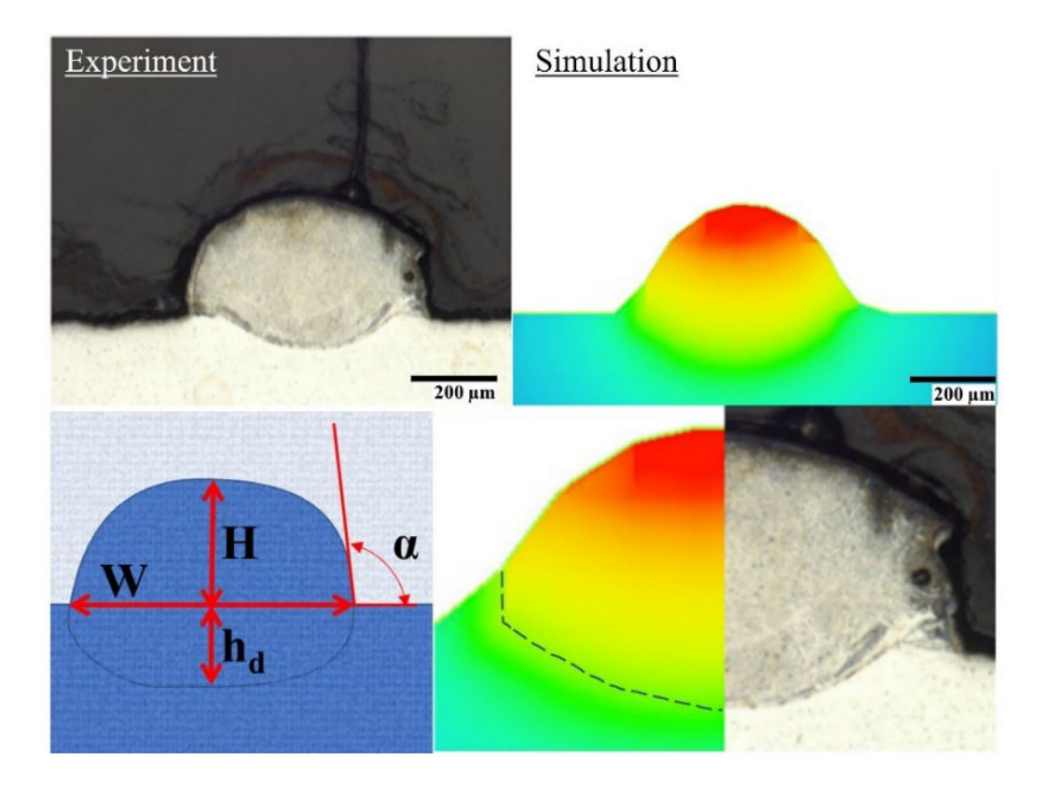




Table 5 Cross-sectional parameter comparison between the experiment and the simulation

Parameters	Experimental value	Simulation value
Н	~265 µm	~245 μm
h_d	~72 μm	~75 µm
W	~535 µm	~580 µm
α	~98°	~110°

temperature distributions during the deposition process are followed by the cooling curve in which the temperature drops exponentially below 400 K after a minute of cooling. This temperature further drops below 350 K and reaches 303 K at the end of 5 min of cooling. The residual stress σ_{11} in the as-built DED layer is measured at 3 different locations as shown in Fig. 8 and at 5 different cooling timeframes. Because of the continuous melt pool creation at each time step, the residual stresses observed are predominantly tensile.

Fig. 8 The analogous DED deposition direction and the UNSM scanning direction (red continuous line) and the different paths 1, 2, and 3 at the depth location (black continuous line) considered to measure residual stress before and after the UNSM process

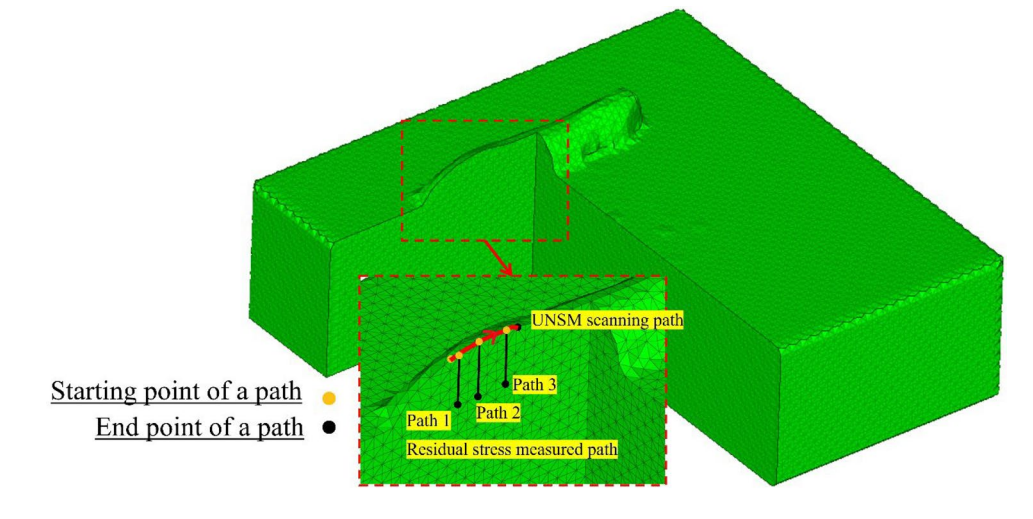


Fig. 9 Residual stress before UNSM (left) and after UNSM (right) at path 1 depicting the effect of the UNSM at the starting position of the overall UNSM scanning distance

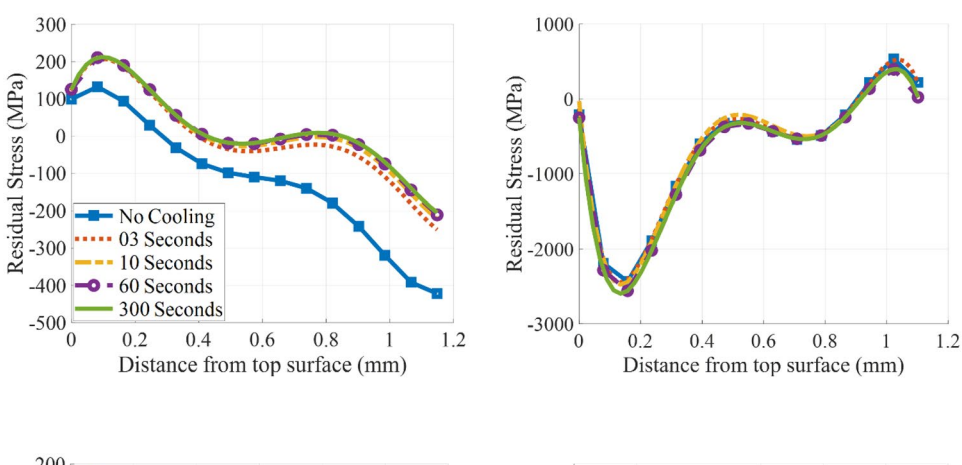


Fig. 10 Residual stress before UNSM (left) and after UNSM (right) at path 2 which represents the mid-position of the overall UNSM scanning distance

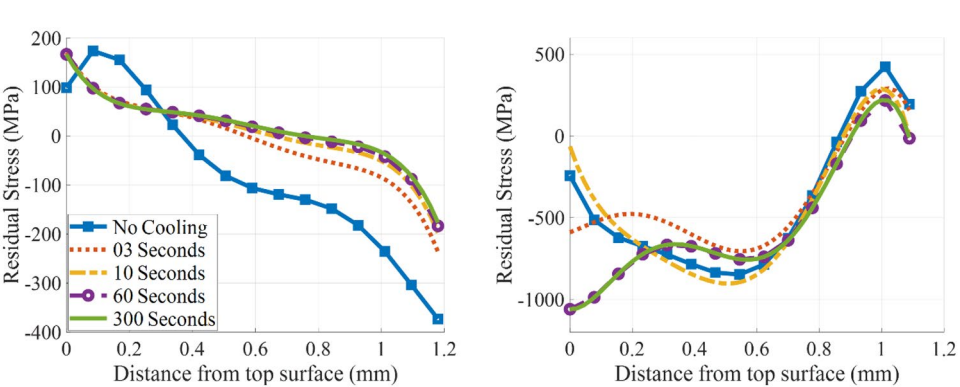
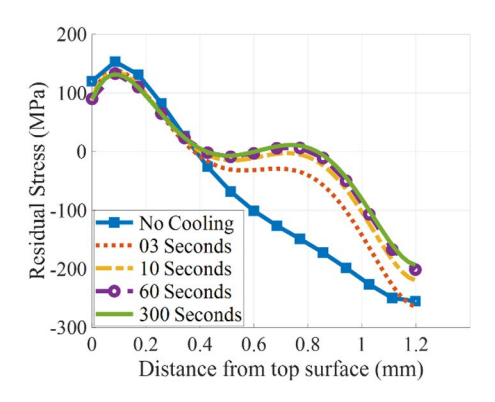
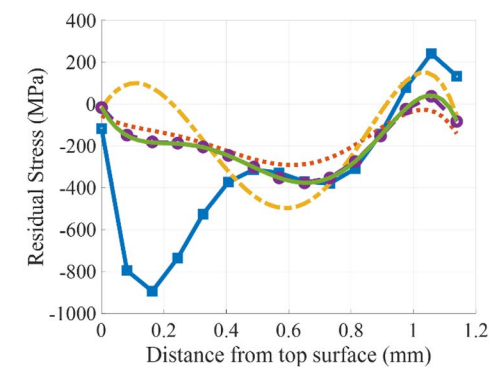




Fig. 11 Residual stress before UNSM (left) and after UNSM (right) at path 3 depicting the effect of the UNSM process at the end of the overall UNSM scanning distance





The accumulated tensile residual stress in the DED built single layer magnitude is shown in Figs. 9, 10 and 11 (left) and varies from ~70 to ~250 MPa for up to a depth of maximum of ~400 µm of the total ~1100 µm layer height. The region covered under the tensile residual stress is relatively large compared to the small regions covered with compressive residual stress towards the substrate. The compressive residual stress at the interface between the layer and the substrate provides resistance to debonding failure. These results show the importance to mitigate the tensile residual stress in the DED built layer before the deposition of the successive layer. Hence, the effect of the UNSM on the built layer is further identified.

The residual stress profiles after the UNSM treatment are measured at the same 3 paths that were considered for the residual stress observations after the DED simulation. It should be noted that in Figs. 9, 10 and 11, the UNSM effect is recorded within the DED-built which has an overall height of ~1.1 mm. Therefore, the last point on these plots indicates the interface between the DED-built and the substrate. At the depth location, these paths represent the start of the UNSM tool movement, the end of the UNSM tool movement, and the middle path in-between the two extreme paths. The peak tensile residual stress from the DED built layer is observed to be converted into maximum compressive stress. Also, the surrounding region of the UNSM treatment has been shifted

to a compressive stress region. This shifting is observed to almost 60–80% of the total height of the layer deposited. The net effect of this is that the compressive stress region at the interface between the layer and the substrate remains compressive, and hence, UNSM does not induce any failure to the layer built. Another aspect observed is that UNSM not only induces the compressive stress region through plastic deformation but also helps improve the surface of the layer built.

The effect of UNSM surface treatment on the deposited surface across the 3 paths is illustrated in Figs. 9, 10 and 11 (right). At the location, ~50 μm depth below the top surface, the net effect of the UNSM is higher than at the surface level. Its effect further covered almost 80% of the total layer height at path 1 (Fig. 9, right) of the three depth locations. Continuing further, at path 2 (Fig. 10, right), the UNSM has its highest effect when it is applied after 300 s of cooling, whereas at path 3 (Fig. 11, right), the effect of the UNSM is higher after 60 s of cooling. Overall, the net effect of the UNSM after 60 s of cooling of the DED single layer has reached its peak magnitude not only at the 3 different paths considered, but also at the surface level, and the depth of 50 µm below the surface level path. The 3D contours of the residual stress in the single-layer DED deposited and UNSM treated after 60 s of cooling of the DED deposited layer are shown in Fig. 12. This effect remains consistent throughout

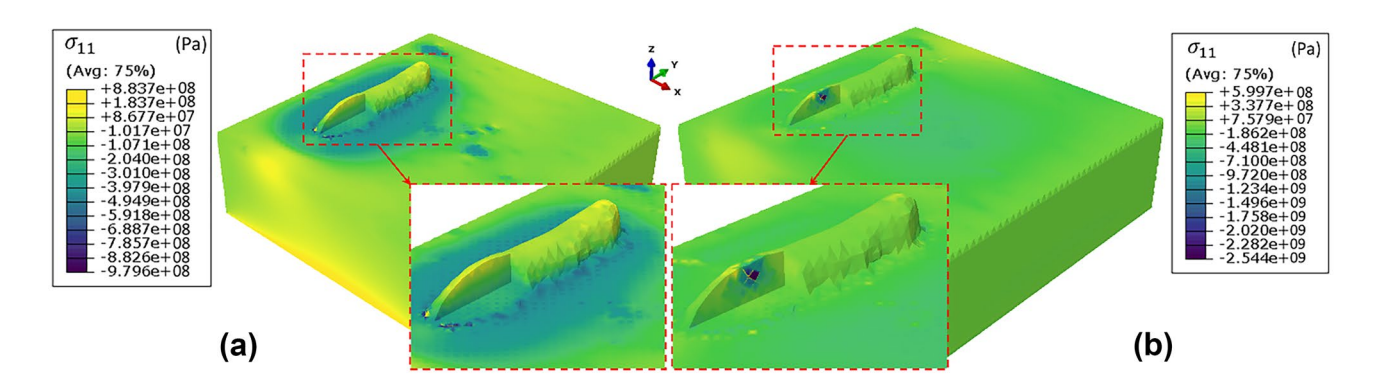


Fig. 12 The 3D contours of the single-layer DED-UNSM processed deposition and the substrate depicting **a** the residual stress after the DED deposition process and **b** the effect of UNSM treatment on the DED build single layer with 60 s cooling



the rest of the cooling period till 300 s. It is also observed that the net effect among the three different paths is different. This is primarily due to the short scanning path of UNSM (1 mm) employed in the simulation. Of the three paths that are chosen, one is close to the start position of the UNSM, another one is close to the end position of the UNSM, and the last one is in between. Therefore, it is expected that the two paths close to the start/end positions will demonstrate different net effects compared to the path in the center.

4 Conclusion

In summary, an in situ integration of the UNSM with the DED process is reported and studied. This integration leads to reduced processing time and more control of the residual stress. This technique stands out as compared to other post-processing techniques such as laser shock peening, and heat-treatment processes. As shown from the computational study, UNSM converts the tensile residual stress region to a compressive residual stress region at a high depth level. Furthermore, the multi-scale simulation strategy for the hybrid DED-UNSM process answers a few fundamental questions.

At first, based on the simulation results, the residual stresses in the DED simulation are time-dependent and depend on the transient temperature distribution. These stresses throughout the deposition and at the cooling stages evolve and accumulate. As observed in the results, these accumulated stresses are predominantly tensile both at the surface level and at the depth level up to ~400 µm deep. The tensile stress region in all 3 observed locations covers more than 40–60% of the total layer thickness of \sim 1100 μ m. To address the issue of the tensile residual stress, the UNSM offers the best adaptable surface treatment at each layer of the DED deposition. This simulation strategy clearly shows the high level of possibility for the integration of the UNSM technique with the DED process to create the hybrid manufacturing capability. This hybrid model accurately predicts the surface geometry of the DED deposited layer and transient temperature distribution. It also successfully demonstrates the positive in situ effect of the UNSM over the DED layer.

The need for surface treatment at each layer of the DED deposition can be effectively carried out by the UNSM technique. Also, the hybrid model provides a detailed insight into the timing of the UNSM application over the DED layer. In the numerical example shown, the net effect of the UNSM reaches the highest in the DED layer with a minimum of 60 s of cooling. Overall, the DED-UNSM hybrid technology can lead to a sustainable DED process that can form sustainable designs. The computational model provides important guidance on building a hybrid technique throughout the layer and layer by layer.

Overall, in the current computational approach that we have developed, the effects of the UNSM are predicted using the implicit finite element method. In the current implementation, the computational expense for capturing the mechanical response at the time scale of seconds to minutes is relatively high due to use of implicit finite element method. In the future, a more efficient simulation method can be developed by using semi-analytical approaches such as those based on the eigen-strain approach [62], and methods that take advantage of the symmetry [63].

Funding Lu received financial support from NSF, DE-NA0003962 and DE-NA-0003525, under CMMI-1726435, and the Louis A. Beecherl Jr. endowed chair. Qian also received financial support from NSF under CMMI-1335204.

Data availability Since the data is part of an ongoing study, it cannot be shared to reproduce the results.

Declarations

Ethics approval Not applicable.

Consent to participate Not applicable.

Consent to publication Authors have agreed and provided consent for the published version of the manuscript.

Competing interests The authors declare no competing interests.

References

- Li W, Soshi M (2019) Modeling analysis of grain morphologies in directed energy deposition (DED) coating with different laser scanning patterns. Mater Lett 251:8–12. https://doi.org/10.1016/j. matlet.2019.05.027
- Gharbi M, Peyre P, Gorny C et al (2013) Influence of various process conditions on surface finishes induced by the direct metal deposition laser technique on a Ti-6Al-4V alloy. J Mater Process Technol 213:791–800. https://doi.org/10.1016/j.jmatprotec.2012.11.015
- Tabernero I, Lamikiz A, Martínez S et al (2012) Modelling of energy attenuation due to powder flow-laser beam interaction during laser cladding process. J Mater Process Technol 212:516–522. https://doi.org/10.1016/j.jmatprotec.2011.10.019
- Zhi'En ET, Pang JHL (2021) Kaminski J Directed energy deposition build process control effects on microstructure and tensile failure behaviour. J Mater Process Technol 294:117139. https://doi.org/10.1016/j.jmatprotec.2021.117139
- Mazumder J, Dutta D, Kikuchi N, Ghosh A (2000) Closed loop direct metal deposition: art to part. Opt Lasers Eng 34:397–414. https://doi.org/10.1016/S0143-8166(00)00072-5
- Chen Y, Clark SJ, Huang Y et al (2021) In situ X-ray quantification of melt pool behaviour during directed energy deposition additive manufacturing of stainless steel. Mater Lett 286:129205. https://doi.org/10.1016/j.matlet.2020.129205
- Shiomil M, Osakadal K, Nakamural K et al (2004) Residual stress within metallic model made by selective laser melting process. CIRP 53:195–198. https://doi.org/10.1016/S0007-8506(07)60677-5



- Mercelis P, Kruth JP (2006) Residual stresses in selective laser sintering and selective laser melting. Rapid Prototyp J 12:254– 265. https://doi.org/10.1108/13552540610707013
- Buchbinder D, Meiners W, Pirch N et al (2014) Investigation on reducing distortion by preheating during manufacture of aluminum components using selective laser melting. J Laser Appl 26:012004. https://doi.org/10.2351/1.4828755
- Lu X, Lin X, Chiumenti M et al (2019) Residual stress and distortion of rectangular and S-shaped Ti-6Al-4V parts by directed energy deposition: modelling and experimental calibration. Addit Manuf 26:166–179. https://doi.org/10.1016/j.addma.2019.02.001
- Lu X, Chiumenti M, Cervera M et al (2021) Substrate design to minimize residual stresses in directed energy deposition AM processes. Mater Des 202:109525. https://doi.org/10.1016/j.matdes. 2021.109525
- Sridharan N, Bunn J, Kottman M et al (2021) Consumable development to tailor residual stress in parts fabricated using directed energy deposition processes. Addit Manuf 39:101837. https://doi. org/10.1016/j.addma.2021.101837
- Jarred CH (2015) Thermo-mechanical model development and experimental validation for directed energy deposition additive manufacturing processes. Dissertation, The Pennsylvania State University
- Wang Z, Palmer TA, Beese AM (2016) Effect of processing parameters on microstructure and tensile properties of austenitic stainless steel 304L made by directed energy deposition additive manufacturing. Acta Mater 110:226–235. https://doi.org/10. 1016/j.actamat.2016.03.019
- Berumen S, Bechmann F, Lindner S et al (2010) Quality control of laser- and powder bed-based Additive Manufacturing (AM) technologies. Phys Procedia 5:617–622
- Tapia G, Elwany A (2014) A review on process monitoring and control in metal-based additive manufacturing. J Manuf Sci E T ASME. https://doi.org/10.1115/1.4028540
- Alimardani M, Fallah V, Iravani-Tabrizipour M, Khajepour A (2012) Surface finish in laser solid freeform fabrication of an AISI 303L stainless steel thin wall. J Mater Process Technol 212:113–119. https://doi.org/10.1016/j.jmatprotec.2011.08.012
- Stender M, Beghini L, Sugar J et al (2018) A thermal-mechanical finite element workflow for directed energy deposition additive manufacturing process modeling. Addit Manuf 21:556–566. https://doi.org/10.1016/j.addma.2018.04.012
- Liu FQ, Wei L, Shi SQ, Wei HL (2020) On the varieties of build features during multi-layer laser directed energy deposition. Addit Manuf 36:101491. https://doi.org/10.1016/j.addma.2020.101491
- Dong JX, Xie XS, Zhang SH (1993) Enhancements of thermal structure stability in a Ni-base superalloy. Scr Metall Mater 28:1477–1482
- Kreitcberg A, Brailovski V, Turenne S (2017) Effect of heat treatment and hot isostatic pressing on the microstructure and mechanical properties of Inconel 625 alloy processed by laser powder bed fusion. Mater Sci Eng A 689:1–10. https://doi.org/10.1016/j.msea. 2017.02.038
- Luo KY, Jing X, Sheng J et al (2016) Characterization and analyses on micro-hardness, residual stress and microstructure in laser cladding coating of 316L stainless steel subjected to massive LSP treatment. J Alloy Compd 673:158–169. https:// doi.org/10.1016/j.jallcom.2016.02.266
- Chi J, Cai Z, Zhang H et al (2021) Combining manufacturing of titanium alloy through direct energy deposition and laser shock peening processes. Mater Des. https://doi.org/10.1016/j.matdes. 2021.109626
- Sealy MP, Madireddy G, Li C, Guo YB (2016) Finite element modeling of hybrid additive manufacturing by laser shock peening. Solid Freeform Fabrication: Proceedings of the 27th Annual International

- Kalentics N, Boillat E, Peyre P et al (2017) Tailoring residual stress profile of selective laser melted parts by laser shock peening. Addit Manuf 16:90–97. https://doi.org/10.1016/j.addma. 2017.05.008
- Gong Y, Li P (2019) Analysis of tool wear performance and surface quality in post milling of additive manufactured 316L stainless steel. J Mech Sci Technol 33:2387–2395. https://doi. org/10.1007/s12206-019-0237-x
- 27. Farayibi PK, Abioye TE, Murray JW et al (2015) Surface improvement of laser clad Ti-6Al-4V using plain waterjet and pulsed electron beam irradiation. J Mater Process Technol 218:1–11. https://doi.org/10.1016/j.jmatprotec.2014.11.035
- Venkatesan K, Ramanujam R, Kuppan P (2014) Analysis of cutting forces and temperature in laser assisted machining of inconel 718 using taguchi method. Procedia Eng 97:1637–1646
- Schopphoven T, Gasser A, Wissenbach K, Poprawe R (2016) Investigations on ultra-high-speed laser material deposition as alternative for hard chrome plating and thermal spraying. J Laser Appl 28:022501. https://doi.org/10.2351/1.4943910
- 30. Kalentics N, de Seijas MOV, Griffiths S et al (2020) 3D laser shock peening A new method for improving fatigue properties of selective laser melted parts. Addit Manuf. https://doi.org/10.1016/j.addma.2020.101112
- Kalentics N, Sohrabi N, Tabasi HG et al (2019) Healing cracks in selective laser melting by 3D laser shock peening. Addit Manuf. https://doi.org/10.1016/j.addma.2019.100881
- Kalentics N, Burn A, Cloots M, Logé RE (2019) 3D laser shock peening as a way to improve geometrical accuracy in selective laser melting. Int J Adv Manuf Technol 101:1247–1254. https:// doi.org/10.1007/s00170-018-3033-3
- Kalentics N, Boillat E, Peyre P et al (2017) 3D Laser shock peening — a new method for the 3D control of residual stresses in selective laser melting. Mater Des 130:350–356. https://doi. org/10.1016/j.matdes.2017.05.083
- Kalentics N, Huang K, Varela O, de Seijas M et al (2019) Laser shock peening: a promising tool for tailoring metallic microstructures in selective laser melting. J Mater Process Technol 266:612–618. https://doi.org/10.1016/j.jmatprotec.2018.11.024
- Amanov A, Cho IS, Kim DE, Pyun YS (2012) Fretting wear and friction reduction of CP titanium and Ti-6Al-4V alloy by ultrasonic nanocrystalline surface modification. Surf Coat Technol 207:135–142. https://doi.org/10.1016/j.surfcoat.2012.06.046
- Khan MK, Fitzpatrick ME, Wang QY et al (2018) Effect of ultrasonic nanocrystal surface modification on residual stress and fatigue cracking in engineering alloys. Fatigue Fract Eng Mater Struct 41:844–855. https://doi.org/10.1111/ffe.12732
- Cao XJ, Pyoun YS, Murakami R (2010) Fatigue properties of a S45C steel subjected to ultrasonic nanocrystal surface modification. Appl Surf Sci 256:6297–6303. https://doi.org/10.1016/j. apsusc.2010.04.007
- 38. Kheradmandfard M, Kashani-Bozorg SF, Kim CL et al (2017) Nanostructured β-type titanium alloy fabricated by ultrasonic nanocrystal surface modification. Ultrason Sonochem 39:698–706. https://doi.org/10.1016/j.ultsonch.2017.03.061
- 39. Cherif A, Pyoun Y, Scholtes B (2010) Effects of ultrasonic nanocrystal surface modification (UNSM) on residual stress state and fatigue strength of AISI 304. J Mater Eng Perform 19:282–286. https://doi.org/10.1007/s11665-009-9445-3
- Khan MK, Liu YJ, Wang QY et al (2016) Effect of ultrasonic nanocrystal surface modification on the characteristics of AISI 310 stainless steel up to very high cycle fatigue. Fatigue Fract Eng Mater Struct 39:427–438. https://doi.org/10.1111/ffe.12367
- Gill A, Telang A, Mannava SR et al (2013) Comparison of mechanisms of advanced mechanical surface treatments in nickel-based superalloy. Mater Sci Eng, A 576:346–355. https://doi.org/10.1016/j.msea.2013.04.021



- Kim MS, Park SH, Pyun YS, Shim DS (2020) Optimization of ultrasonic nanocrystal surface modification for surface quality improvement of directed energy deposited stainless steel 316L. J Market Res 9:15102–15122. https://doi.org/10.1016/j.jmrt.2020. 10.092
- Kim MS, Jo YK, Park SH, Shim DS (2019) Application of ultrasonic nanocrystal surface modification for improving surface profile of DEDed AISI 316L. J Mech Sci Technol 33:5659–5667. https://doi.org/10.1007/s12206-019-1108-1
- Kim MS, Oh WJ, Baek GY et al (2020) Ultrasonic nanocrystal surface modification of high-speed tool steel (AISI M4) layered via direct energy deposition. J Mater Process Technol 277:116420. https://doi.org/10.1016/j.jmatprotec.2019.116420
- 45. Sidhu KS (2018) Residual stress enhancement of additively manufactured Inconel 718 by laser shock peening and ultrasonic nanocrystal surface modification. Thesis, The University of Cincinnati
- Cho IS, Lee CS, Choi CH et al (2017) Effect of the ultrasonic nanocrystalline surface modification (UNSM) on bulk and 3D-printed AISI H13 tool steels. Metals. https://doi.org/10.3390/ met7110510
- Mills KC (2002) Recommended values of thermophysical properties for selected commercial alloys. Woodhead Publishing Ltd, Cambridge, England
- Flow Science.Inc FLOW-3D 2022 R1. https://www.flow3d.com/ products/flow-3d/flow-3d-2022r1/. Accessed 7 Mar 2022
- Wen SY, Shin YC, Murthy JY, Sojka PE (2009) Modeling of coaxial powder flow for the laser direct deposition process. Int J Heat Mass Transf 52:5867–5877. https://doi.org/10.1016/j. iiheatmasstransfer.2009.07.018
- 50. Lee Y (2015) Simulation of laser additive manufacturing and its applications. Dissertation, The Ohio State University
- Gürtler FJ, Karg M, Leitz KH (2013) Schmidt M Simulation of laser beam melting of steel powders using the three-dimensional volume of fluid method. Phys Procedia 41:881–886. https://doi. org/10.1016/j.phpro.2013.03.162
- Hirt CW, Nichols BD (1981) Volume of Fluid (VOF) Method for the dynamics of free boundaries. J Comput Phys 39:201–225. https://doi.org/10.1016/0021-9991(81)90145-5
- 53. Saldi ZS (2011) Marangoni driven free surface flows in liquid weld pools. Delft University of Technology, Thesis

- Zhang YM, Lim CWJ, Tang C, Li B (2021) Numerical investigation on heat transfer of melt pool and clad generation in directed energy deposition of stainless steel. Int J Therm Sci. https://doi.org/10.1016/j.ijthermalsci.2021.106954
- Zhu G, Li D, Zhang A et al (2012) The influence of laser and powder defocusing characteristics on the surface quality in laser direct metal deposition. Opt Laser Technol 44:349–356. https:// doi.org/10.1016/j.optlastec.2011.07.013
- de Freitas R, Teixeira P, Bezerra de Araújo D, Bragança A, da Cunha L (2014) Study of the gaussian distribution heat source model applied to numerical thermal simulations of TIG welding processes. Science & Engineering Journal 23:115–122
- Karkalos NE, Markopoulos AP (2018) Determination of Johnson-Cook material model parameters by an optimization approach using the fireworks algorithm. Procedia Manufacturing 22:107– 113. https://doi.org/10.1016/j.promfg.2018.03.017
- Dassault Systèmes (2021) ABAQUS 2021. https://www.3ds.com/ products-services/simulia/products/abaqus/. Accessed 7 Mar 2022
- Amanov A, Lee SW, Pyun YS (2017) Low friction and high strength of 316L stainless steel tubing for biomedical applications. Mater Sci Eng, C 71:176–185. https://doi.org/10.1016/j. msec.2016.10.005
- Miedzinski M (2017) Materials for additive manufacturing by direct energy deposition. Chalmers University of Technology, Thesis
- Balit Y (2019) Mechanical properties of additively manufactured or repaired single-track thickness structures by Directed Energy Deposition. Dissertation, The Polytechnic Institute of Paris
- Jun TS, Korsunsky AM (2010) Evaluation of residual stresses and strains using the Eigenstrain Reconstruction Method. Int J Solids Struct 47:1678–1686. https://doi.org/10.1016/j.ijsolstr.2010.03. 002
- Hu Y, Yao Z (2008) Numerical simulation and experimentation of overlapping laser shock processing with symmetry cell. Int J Mach Tools Manuf 48:152–162. https://doi.org/10.1016/j.ijmachtools. 2007.08.021

Publisher's Note Springer Nature remains neutral with regard to jurisdictional claims in published maps and institutional affiliations.

